https://doi.org/10.5194/egusphere-2026-2476
Preprint. Discussion started: 29 May 2026

Direct Radar Reflectivity Assimilation within MPAS-JEDI using Reflectivity Analysis Variable and Multivariate Background Error Covariance

Tao Sun[1], I-Han Chen[1], Craig S. Schwartz[2], Zhiquan Liu[2], Hugh Zhang[1], Dale Barker[1]

[1]Centre for Climate Research Singapore, 537054, Singapore
[2]NSF National Center for Atmospheric Research, Boulder, 80301, United States

Correspondence to: Tao Sun (tao_sun@nea.gov.sg)

Abstract. This study implements direct reflectivity assimilation within the Joint Effort for Data assimilation Integration (JEDI) with the Model for Prediction Across Scales–Atmosphere (MPAS-A) (i.e., MPAS-JEDI) and evaluates its performance for hourly cycled radar assimilation in heavy rainfall forecasts over the deep tropics. Radar reflectivity observations are directly assimilated using the hybrid 3DEnVar method, in which reflectivity is treated as an analysis variable. Multivariate correlations between reflectivity and temperature, humidity, and hydrometeors are incorporated into the static component of the background error covariance (BEC), allowing reflectivity information to propagate to the model state variables. In addition, reflectivity states are updated from the analyzed hydrometeors across successive outer loops, seeking improved consistency between reflectivity and hydrometeor fields and a better fit to the reflectivity observations. Diagnosis of the multivariate BEC reveals physically consistent cross-variable correlations among thermodynamic, microphysical, and reflectivity fields. Single observation assimilation tests demonstrate that direct reflectivity assimilation effectively propagates reflectivity increments to both hydrometeor and thermodynamic variables. Results from a Sumatra squall line case indicate that updating reflectivity from analyzed hydrometeors across successive outer loops produces a closer fit to observed reflectivity and improves the forecast accuracy of the squall-line system. Furthermore, the hybrid multivariate BEC outperforms the ensemble-based BEC in reflectivity assimilation by substantially improving the analyses of dynamical and microphysical states, leading to better predictions of squall-line intensity, orientation, and propagation. The multi-case quantitative evaluation further demonstrates the superiority of hybrid multivariate BEC over the ensemble-based BEC in improving both composite reflectivity and 3-h accumulated precipitation forecasts over the Singapore region. Overall, the successful implementation of direct reflectivity assimilation in MPAS-JEDI highlights the added value of incorporating a multivariate BEC for improving heavy rainfall prediction in the deep tropics.

1 Introduction

Accurately predicting severe weather events, such as supercells, tornadoes, squall-lines, and heavy rainfall, remains a critical challenge for both research and operational numerical weather prediction (NWP). Doppler weather radars provide high-

https://doi.org/10.5194/egusphere-2026-2476
Preprint. Discussion started: 29 May 2026

resolution observations of radial velocity and reflectivity, capturing the dynamic and microphysical structures of severe storms with good temporal and spatial coverage. The assimilation of these observations substantially improves the initial conditions of NWP models at convective scale, thereby enhancing short-range severe weather forecasts (Kain et al. 2010; Sun et al. 2012). However, the direct assimilation of radar reflectivity with the variational data assimilation (DA) method remains challenging (Liu et al. 2020).

Direct assimilation of radar reflectivity requires an observation operator to link reflectivity to model state variables. Variational DA methods, which are typically based on the incremental framework (Courtier et al. 1994), also necessitate the construction of the tangent linear (TL) and adjoint (AD) of the reflectivity operator. Considerable effort has gone into developing reflectivity and its TL and AD operators for variational DA methods (Sun and Crook 1997; Xiao et al. 2007; Gao and Stensrud 2012; Wang and Liu 2019; Liu et al. 2022; Liu et al. 2025; Tong et al. 2020; Park et al. 2026). In practice, these operators are often simplified, which can introduce representativeness errors and inconsistencies with the underlying microphysical schemes. Furthermore, the strong nonlinearity of reflectivity complicates its direct variational assimilation. For example, Sun and Crook (1997) demonstrated that a large gradient arising from small errors in mixing ratios of hydrometeors can severely degrade the conditioning of the cost function and substantially slow its minimization. Furthermore, Wang et al. (2013) showed that, when the background state is too dry, linearization errors in the reflectivity operator tend to produce pronounced dry biases in the analysis. To mitigate the nonlinearity issues, previous studies have explored different control variable transforms, such as the logarithmic transform or power transform of hydrometeors (Chen et al., 2021; Liu et al., 2022), and evaluated the impact of assimilating reflectivity observations on a logarithmic scale or using power-transformed variables (Liu et al. 2025). There is still room for improvement.

Conversely, in Ensemble Kalman Filter (EnKF; Evensen 1994)-based DA methods, complex and nonlinear reflectivity operators can be easily implemented without requiring their TL and AD operators. Reflectivity observations can influence other model state variables via the multivariate correlations represented in the ensemble-based background error covariance (BEC). Numerous studies have demonstrated the effectiveness of EnKF-based methods for directly assimilating radar reflectivity in severe weather applications (e.g., Tong and Xue 2005; Xue et al. 2010; Dowell et al. 2011; Jung et al. 2012; Stensrud et al. 2013; Snook et al. 2015; Park et al. 2023; Kong et al. 2025). Inspired by these EnKF-based approaches, Wang and Wang (2017) proposed a direct reflectivity assimilation approach within the variational DA framework, in which reflectivity is treated as an analysis variable, and assimilated reflectivity observations impact other state variables through the multivariate correlations derived in the ensemble-based BEC. This method reduces the reflectivity observation operator to an identity operator, thereby avoiding the need for the TL and AD of reflectivity operators and significantly simplifying the implementation of direct reflectivity assimilation within the variational DA framework.

However, when a pure ensemble-based BEC is used, sampling errors due to limited ensemble size can degrade the analysis. To address this issue, Wang and Wang (2021) introduced a hybrid BEC for direct reflectivity assimilation, in which multivariate correlations between reflectivity and other state variables are incorporated into the static component of the BEC, and demonstrated positive impacts on the analysis. Gao et al. (2024) also illustrated the effectiveness of direct reflectivity

https://doi.org/10.5194/egusphere-2026-2476
Preprint. Discussion started: 29 May 2026

assimilation using reflectivity as an analysis variable and a hybrid BEC within the ensemble of data assimilation (EDA) framework, showing improved analyses and short-range forecasts for two severe storm cases.

In this study, we implement the direct reflectivity assimilation approach within MPAS-JEDI (Liu et al. 2022), a next-generation DA system specific for the Model for Prediction Across Scales – Atmosphere (MPAS-A; Skamarock et al. 2012; 2016) within the Joint Effort for Data assimilation Integration (JEDI; Trémolet, 2020) framework. A multivariate BEC is introduced to represent cross-variable correlations between reflectivity and thermodynamic and hydrometeor variables, enabling observed reflectivity to be effectively propagated to both thermodynamic and microphysical states within the hybrid three-dimensional ensemble-variational (3DEnVar) method. In contrast to previous studies focusing on mid-latitude severe weather, relatively few studies have explored direct reflectivity assimilation for deep-tropical environments; this study examines the added value of the multivariate BEC in direct reflectivity assimilation for heavy rainfall prediction in the deep tropics.

The remainder of this paper is organized as follows. Section 2 describes the hybrid 3DEnVar algorithm and multivariate BEC modeling within MPAS-JEDI. Section 3 presents the MPAS-A model configuration, observations, and experimental setup. Section 4 discusses the characteristics of multivariate correlations and validates it through single observation assimilation experiments. Section 5 evaluates the proposed direct reflectivity approach with hourly cycled radar assimilation experiments. A summary and conclusions are provided in section 6.

2 Methodology

2.1 MPAS-JEDI hybrid 3DEnVar

MPAS-JEDI is a DA system developed specifically for the MPAS-A model within the JEDI framework. It interfaces with the Object-Oriented Prediction System (OOPS), which serves as the DA solver component and connects MPAS-JEDI to a suite of model-agnostic components within the JEDI framework. These model-agnostic components include the Unified Forward Operator (UFO), which provides observation operators, observation error modelling, and quality control; the Interface for Observation Data Access (IODA), which handles observation storage and access; and the System-Agnostic Background Error Representation (SABER), within which the BEC is formulated.

The variational DA of OOPS obtains the optimal analysis by minimizing an incremental cost function (Courtier et al. 1994) that measures the misfit between observations and model states, as follows:

$$J(\delta\mathbf{x}) = \frac{1}{2}\left(\delta\mathbf{x} - \delta\mathbf{x}_g\right)^{\mathrm{T}}\mathbf{B}^{-1}\left(\delta\mathbf{x} - \delta\mathbf{x}_g\right) + \frac{1}{2}\{\mathbf{H}\delta\mathbf{x} - \mathbf{d}\}^{\mathrm{T}}\mathbf{R}^{-1}\{\mathbf{H}\delta\mathbf{x} - \mathbf{d}\}, \quad (1)$$

where $\delta\mathbf{x} = \mathbf{x} - \mathbf{x}_g$ is the analysis increment relative to the first guess $\mathbf{x}_g$; $\delta\mathbf{x}_g = \mathbf{x}_b - \mathbf{x}_g$ represents the difference between the background $\mathbf{x}_b$ and the guess $\mathbf{x}_g$; $\mathbf{d} = \mathbf{y}^o - H(\mathbf{x}_g)$ is the innovation vector, i.e., the difference between the observations $\mathbf{y}^o$ and the model equivalents obtained by applying the nonlinear observation operator H to $\mathbf{x}_g$; $\mathbf{H}$ is the linearized version of H; and $\mathbf{B}$ and $\mathbf{R}$ are the BEC matrix and observation error covariance matrix, respectively. Multiple outer loops (OL) are

https://doi.org/10.5194/egusphere-2026-2476
Preprint. Discussion started: 29 May 2026

commonly employed to account for the nonlinearity in $\mathbf{H}$, allowing the solution to progressively converge toward the optimal analysis. In each OL, the guess $\mathbf{x}_g$ is updated using the analysis from the previous OL, except in the first OL where $\mathbf{x}_g = \mathbf{x}_b$; $\mathbf{d}$ is recalculated from the updated $\mathbf{x}_g$.

2.2 Hybrid BEC of MPAS-JEDI

The modeling of the $\mathbf{B}$ matrix is a key component of variational DA and leads to different algorithmic variants. In this study, the hybrid 3DEnVar method is employed, in which $\mathbf{B}$ is a weighted sum of the ensemble-based BEC matrix $\mathbf{B}_e$ and the static BEC matrix $\mathbf{B}_s$:

$$\mathbf{B} = \beta_s \mathbf{B}_s + \beta_e \mathbf{B}_e, \quad (2)$$

where β_s and β_e are the scalar weights satisfying $\beta_s + \beta_e = 1$.

Following Liu et al. (2022), the ensemble-based BEC matrix $\mathbf{B}_e$ of MPAS-JEDI is formulated as a localized covariance matrix:

$$\mathbf{B}_e = \frac{1}{N_e - 1} \mathbf{L} \circ (\mathbf{X}\mathbf{X}^{\mathrm{T}}), \quad (3)$$

where N_e is ensemble size, $\mathbf{X}$ is the ensemble perturbation matrix whose columns are deviations of the ensemble members from the ensemble mean, and $\mathbf{L}$ is the covariance localization matrix applied through the Schur (element-wise) product ($\circ$) to suppress spurious long-range correlations. This ensemble-based BEC provides flow-dependent and multivariate covariances, allowing the observational information to propagate from observed variables to unobserved variables through cross-variable correlations embedded in the ensemble perturbations.

Following Jung et al. (2024), the static BEC matrix $\mathbf{B}_s$ of MPAS-JEDI is expressed as follows:

$$\mathbf{B}_s = \mathbf{K}_1 \mathbf{K}_2 \mathbf{\Sigma C \Sigma}^{\mathrm{T}} \mathbf{K}_2{}^{\mathrm{T}} \mathbf{K}_1{}^{\mathrm{T}}. \quad (4)$$

In the center of $\mathbf{B}_s$, the block-diagonal covariance $\mathbf{\Sigma C \Sigma}^T$ is formulated as the product of a block-diagonal correlation matrix $\mathbf{C}$ and a diagonal matrix $\mathbf{\Sigma}$, defined in the control-variable space. The control variables are the quantities optimized during the minimization and are defined prior to the application of the vertical balance operator $\mathbf{K}_2$, where they are assumed to be uncorrelated. The blocks of $\mathbf{C}$ provide the univariate horizontal and vertical correlations for each control variable, while the diagonal elements of $\mathbf{\Sigma}$ specify the corresponding standard deviations. A detailed description of the $\mathbf{\Sigma C \Sigma}^{\mathrm{T}}$ formulation can be found in Jung et al. (2024). Through the vertical balance operator $\mathbf{K}_2$, these control variables are transformed into multivariate, physically balanced analysis variables. This operator is the primary focus of this study and is described in detail in Section 2.3. The operator $\mathbf{K}_1$ is a linear variable transform that converts increments of the balanced analysis variables (output of $\mathbf{K}_2$) into increments of the model-space analysis variables; in this study, $\mathbf{K}_1$ is taken as the identity operator.

2.3 Multivariate correlation

Previous studies have demonstrated that reflectivity assimilation using a multivariate BEC (hereafter referred to as MBE), which explicitly accounts for cross-variable correlation between reflectivity-related variables and the other state variables,

https://doi.org/10.5194/egusphere-2026-2476
Preprint. Discussion started: 29 May 2026

leads to improved initial conditions and enhanced short-range forecast accuracy (e.g. Wang and Wang 2021; Zheng et al. 2023; Chen et al, 2024).

In this study, the cross-variable correlations are established through the vertical balance operator $\mathbf{K}_2$, implemented within the Background error on Unstructured Mesh Package (BUMP) in SABER. The analysis variables selected include zonal-wind (U) and meridional-wind (V) components, temperature (T), specific humidity (Q), surface pressure (P_s), and mixing ratios of cloud water (Q_c), ice (Q_i), rainwater (Q_r), snow (Q_s), and graupel (Q_g), as well as radar reflectivity (Z_h). The multivariate correlations are constructed in $\mathbf{K}_2$ as

$$\begin{bmatrix} \delta U \\ \delta V \\ \delta T \\ \delta Q \\ \delta P_s \\ \delta Q_c \\ \delta Q_i \\ \delta Q_r \\ \delta Q_s \\ \delta Q_g \\ \delta Z_h \end{bmatrix} = \begin{bmatrix} \mathrm{I} & 0 & 0 & 0 & 0 & 0 & 0 & 0 & 0 & 0 & 0 \\ 0 & \mathrm{I} & 0 & 0 & 0 & 0 & 0 & 0 & 0 & 0 & 0 \\ 0 & 0 & \mathrm{I} & \mathrm{C}_{T_\mathrm{u},Q_\mathrm{u}} & 0 & 0 & 0 & 0 & 0 & 0 & \mathrm{C}_{T_\mathrm{u},Z_h} \\ 0 & 0 & 0 & \mathrm{I} & 0 & 0 & 0 & 0 & 0 & 0 & \mathrm{C}_{Q_u,Z_h} \\ 0 & 0 & 0 & 0 & \mathrm{I} & 0 & 0 & 0 & 0 & 0 & 0 \\ 0 & 0 & 0 & 0 & 0 & \mathrm{I} & 0 & 0 & 0 & 0 & \mathrm{C}_{Qc_\mathrm{u},Z_h} \\ 0 & 0 & 0 & 0 & 0 & 0 & \mathrm{I} & 0 & 0 & 0 & \mathrm{C}_{Qi_\mathrm{u},Z_h} \\ 0 & 0 & 0 & 0 & 0 & 0 & 0 & \mathrm{I} & 0 & 0 & \mathrm{C}_{Qr_\mathrm{u},Z_h} \\ 0 & 0 & 0 & 0 & 0 & 0 & 0 & 0 & \mathrm{I} & 0 & \mathrm{C}_{Qs_\mathrm{u},Z_h} \\ 0 & 0 & 0 & 0 & 0 & 0 & 0 & 0 & 0 & \mathrm{I} & \mathrm{C}_{Qg_\mathrm{u},Z_h} \\ 0 & 0 & 0 & 0 & 0 & 0 & 0 & 0 & 0 & 0 & \mathrm{I} \end{bmatrix} \begin{bmatrix} \delta U \\ \delta V \\ \delta T_u \\ \delta Q_u \\ \delta P_s \\ \delta Q_{c_u} \\ \delta Q_{i_u} \\ \delta Q_{r_u} \\ \delta Q_{s_u} \\ \delta Q_{g_u} \\ \delta Z_h \end{bmatrix}. \quad (5)$$

Through this transformation, the increments of analysis variables —U, V, T, Q, P_s, Q_c, Q_i, Q_r, Q_s, Q_g, and Z_h are derived from the increments of control variables: U, V, unbalanced temperature (T_u), unbalanced specific humidity (Q_u), P_s, unbalanced mixing ratios of cloud water (Q_{c_u}), ice (Q_{i_u}), rainwater (Q_{r_u}), snow (Q_{s_u}), and graupel (Q_{g_u}), and Z_h.

In this formulation, cross-variable correlations are explicitly introduced between reflectivity and temperature, specific humidity, and hydrometeors. Additionally, a temperature–humidity ($T-Q$) correlation is included to compensate for the absence of implicit correlations that would otherwise arise when pseudo–relative humidity is used as the humidity analysis variable. The inclusion of $T-Q$ correlation has shown improvements in assimilating conventional observations and is therefore applied in all DA experiments in this study. Unlike Wang and Wang (2021), cross-correlations involving the wind components (U, V) and P_s with other variables are omitted, as these correlations are generally weak. Furthermore, cross-correlations among different hydrometeor species, as well as between hydrometeors and temperature or specific humidity, are excluded to avoid redundancy with correlations already introduced through reflectivity.

With this multivariate formulation, the static BEC increment of each analysis variable can be decomposed into an unbalanced component (denoted by the subscript "u"), which is independent of other control variables, and a balanced component arising from cross-variable correlations. Taking the temperature increment as an example, the full increment δT is expressed as the sum of its unbalanced component δT_u and the balanced component associated with the increment of unbalanced specific humidity δQ_u and the reflectivity increment δZ_h:

$$\delta T = \delta T_u + C_{T_u,Q_u}\delta Q_u + C_{T_u,Z_h}\delta Z_h, \quad (6)$$

https://doi.org/10.5194/egusphere-2026-2476
Preprint. Discussion started: 29 May 2026

where C_{T_u,Q_u} and C_{T_u,Z_h} are the cross-correlation coefficients linking the balanced component of δT to the unbalanced humidity increment (δQ_u) and reflectivity increment (δZ_h), respectively. Under this formulation, δQ and δZ_h can propagate to δT through the prescribed multivariate cross-correlations. Similarly, δZ_h can propagate to the increments of specific humidity and the five hydrometeor mixing ratios.

Physically, Z_h is directly associated with precipitation hydrometeors (i.e., Q_r, Q_s, and Q_g) and indirectly linked to non-precipitation hydrometers (i.e., Q_c, and Q_i), temperature, and humidity through microphysical processes. By incorporating these cross-variable correlations, the established MBE facilitates dynamically and physically consistent adjustments among thermodynamic and microphysical variables in the analysis, which is particularly important for the direct assimilation of radar reflectivity.

2.4 Direct reflectivity assimilation

When reflectivity is included as an analysis variable, the observation operator H is reduced to a simple interpolation operator that maps the model-simulated reflectivity to the observation locations. Consequently, the construction of TL and AD operators for the nonlinear reflectivity operator itself is no longer required, which significantly simplifies the implementation of direct reflectivity assimilation within the variational framework. Because the nonlinear errors associated with the TL approximation of the reflectivity observation operator are effectively eliminated, Wang and Wang (2017) argued that it is unnecessary to employ multiple OLs for direct reflectivity assimilation.

However, the inherently nonlinear nature of the reflectivity operator poses a fundamental challenge to the linearity assumptions underlying variational frameworks. When reflectivity is treated as an analysis variable, its impact on other model variables relies solely on linearized cross-variable relationships embedded in the BEC. As a result, an improved fit to reflectivity observations does not necessarily translate into physically consistent improvements in the underlying hydrometeor or thermodynamic states, particularly under severe weather conditions where highly nonlinear microphysical processes dominate and cannot be adequately represented by linear correlations. In such situations, direct reflectivity assimilation may become ineffective or even counterproductive.

In this study, the reflectivity state is updated at each OL by recomputing the reflectivity state from the analyzed hydrometeors using the same reflectivity operator employed in the MPAS-A microphysics scheme. With this procedure, both the reflectivity guess and the corresponding innovations are recalculated at each OL. This allows the reflectivity observations to be assimilated relative to an updated reflectivity state that remains consistent with the analyzed hydrometeors, providing a practical approach to partially account for nonlinearity in direct reflectivity assimilation within the variational framework.

https://doi.org/10.5194/egusphere-2026-2476
Preprint. Discussion started: 29 May 2026

2.5 Large-scale Blending

In limited-area NWP models, large-scale fields are often degraded because the restricted model domain and lateral boundary conditions limit the model's ability to maintain large-scale atmospheric variability. To mitigate this issue, a blending technique is commonly used to combine small-scale information from the regional model with large-scale information from another data source, typically global analyses or forecasts, to produce a blended field for initializing the limited-area NWP forecast. To extract the small- and large-scale information, a scale-separation technique needs to be applied to both data sources individually.

Due to MPAS's unstructured mesh, scale-separation methods based on the Fourier transform are not straightforward to implement. Therefore, we employ a novel blending method (https://github.com/weather4evr/mpas_blending.git; last access: 1 May 2026) loosely based on wavelets to perform a scale-separation for fields on MPAS's unstructured mesh. A comprehensive manuscript on this blending method is currently in preparation; here, we provide only a high-level overview, which we believe is sufficient because all DA experiments in this study use the same blending approach. Consequently, blending does not introduce differences among the experiments.

Our blending method involves upscaling fields on MPAS's native mesh through a hierarchy of progressively coarser MPAS meshes. This iterative upscaling procedure is applied to both the data source providing small-scale information (here, MPAS-JEDI backgrounds) and the data source providing large-scale information (here, ECMWF analyses). Specifically, we progressively upscale model variables of MPAS (i.e., U, V, T, Q, and Ps) from both the MPAS forecasts and ECMWF analyses (the latter has been interpolated onto the 3-km MPAS native mesh) to coarser MPAS meshes with horizontal cells of 30 km, 60 km, 120 km, 240 km, and 480 km. This iterative upscaling performs a scale-separation and yields a series of upscaled fields that contain progressively smaller minimum wavelengths of resolved meteorological features for both data sources.

Following this upscaling procedure, differences between fields on consecutive levels of the mesh hierarchy are computed for each data source. These differences represent the amount of information added to a relatively coarse field to obtain the field on the next finer-resolution mesh within the hierarchy. These differences (or perturbations) between hierarchy levels are then used to reconstruct a blended field on the native 3-km MPAS mesh. During this reconstruction, weights ranging between 0 and 1 (and summing to 1) are applied to the perturbations from both data sources for each level of the mesh hierarchy. For example, at a given mesh hierarchy level, a weight of 0.5 means that both data sources contribute equally to the field at the particular wavelength corresponding to that level. By allowing the weights on the perturbations to vary as a function of wavelength (i.e., mesh hierarchy level), information from the two data sources can be blended in a way that preserves the large scales from one dataset and small scales from the other. Our specific weighting yields blended fields that are entirely derived from ECMWF analyses for wavelengths > 480 km and entirely look like the MPAS-JEDI backgrounds for wavelengths < 30 km.

https://doi.org/10.5194/egusphere-2026-2476
Preprint. Discussion started: 29 May 2026

3. Model, Observation, and Experimental design

3.1 MPAS-A model

The non-hydrostatic MPAS-A version 8.3.1 is used as the NWP model, incorporating several modifications including updated greenhouse gas parameters in the radiation scheme and an update of the MYNN boundary layer scheme. Following Chen et al. (2026), the simulation domain of MPAS-A is centered at (1.21oN, 102oE) with a radius of approximately 1120 km, covering Singapore, the Indonesian islands of Sumatra and Java, and the Malay Peninsula (Fig. 1a). The regional quasi-uniform mesh employs a horizontal cell spacing of ~ 3 km and comprises 522,172 horizontal cells and 66 vertical levels extending to a model top at 40 km. The vertical level distribution is illustrated in Fig. 1b. Physical parameterizations follow Chen et al. (2026) and are summarized in Table 1.

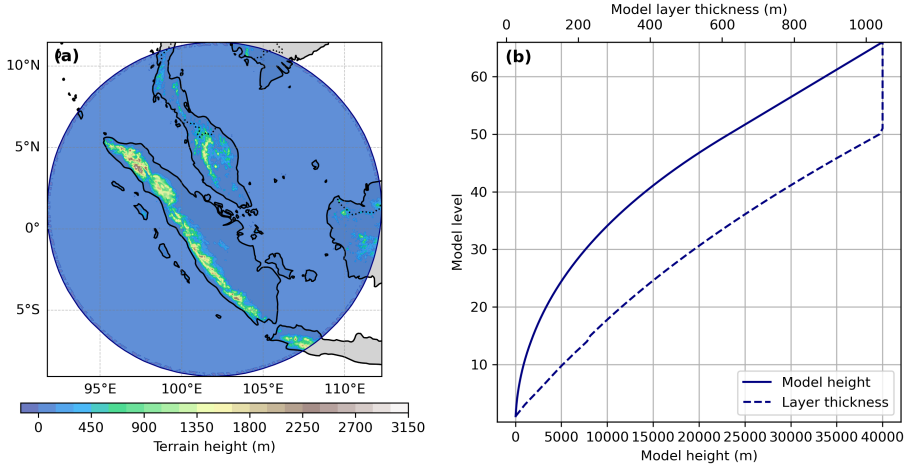

Figure 1. (a) Model simulation domain overlaid with terrain height (shaded; m) and (b) vertical distribution of model mass level height (solid line) and thickness (dashed line).

Table 1. Parameterization scheme configuration.

Parameterization	Scheme
Convection	Grell–Freitas Ensemble Scheme (Grell and Freitas, 2014)
Microphysics	WRF single-moment 6-class Scheme (WSM6; Hong and Lim 2006)
Land surface	Noah Land-Surface Model (Tewari et al. 2004)
Boundary layer	MYNN (Olson et al. 2021)
Surface layer	MYNN (Olson et al. 2021)
Longwave/shortwave Radiation	RRTMG (Iacono et al. 2008)
Cloud fraction for radiation	Xu-Randall (Xu and Randall, 1996)

https://doi.org/10.5194/egusphere-2026-2476
Preprint. Discussion started: 29 May 2026

3.2 Observations

In this study, observations from multiple platforms are assimilated. Conventional observations obtained from the Global Telecommunication System (GTS) include radiosondes (zonal and meridional winds, temperature, and specific humidity), wind profilers (zonal and meridional winds), aircraft (zonal and meridional winds and temperature), atmospheric motion vectors (AMVs; zonal and meridional winds), and surface observations from SYNOP, BUOY, and ship reports (10-m zonal and meridional winds, 2-m temperature, 2-m specific humidity, and surface pressure). Global Navigation Satellite System (GNSS) radio occultation (RO) refractivity observations, which provide good temporal and spatial coverage over the simulation domain, are also assimilated. In addition, radar radial velocity and reflectivity observations from the S-band Changi and C-band Seletar radar sites in Singapore are assimilated; to our knowledge, this is the first time these observations have been assimilated.

Conventional and GNSS RO observations are pre-processed and converted from their native format to the IODA HDF5-based format using the obs2ioda tool (https://github.com/NCAR/obs2ioda; last access: 1 May 2026). For radar radial velocity and reflectivity data, a series of quality control (QC) procedures are applied before conversion to the IODA format, including radial velocity de-aliasing, removal of radar ground clutter, elimination of non-meteorological echoes and outlier reflectivity gates, and attenuation correction for the C-band radar reflectivity data. Following Park et al. (2026), observed reflectivity values below 0 dBZ are treated as “no-rain” echoes and reset to 0 dBZ prior to assimilation to suppress spurious background precipitation. A similar procedure is applied to the model states by resetting simulated reflectivity below 0 dBZ to 0 dBZ to prevent excessively large observation-minus-background (OMB) departures that could otherwise introduce unrealistic analysis increments. The “no-rain” reflectivity data are thinned to approximately 9 km, while reflectivity and radial velocity data associated with precipitation (> 0 dBZ) are thinned to approximately 3 km, comparable to the MPAS-A model cell spacing. After QC and thinning, the radar radial velocity and reflectivity observations are converted to the IODA format.

Both the “PreQC” and “Background Check” filters within UFO are applied to all observations. The “PreQC” filter discards observations with preprocessing-provided quality flags greater than 3. The “Background Check” filter rejects observations whose absolute departures from the background exceed five times the observation error standard deviation for most observation types; for radar data, a more relaxed threshold of ten times the observation error standard deviation is adopted to retain more radar data in assimilation. For surface data, a terrain-height consistency check is applied, and observations are discarded when the difference between model terrain height and station elevation exceeds 200 m. GNSS RO refractivity observations are assimilated only between 2.5 km and the model top at 40 km, owing to larger near-surface bias characteristics. Satellite AMVs are thinned to 30 km to account for spatial correlations among nearby observations. For radar observations, the observation error standard deviation for radial velocity and reflectivity are set to 1.5 m s^{-1} and 3 dBZ, respectively.

https://doi.org/10.5194/egusphere-2026-2476
Preprint. Discussion started: 29 May 2026

3.3 Experimental design

The DA system used in this study is MPAS-JEDI version 3.0.3, with the hybrid 3DEnVar employed as the DA method. Several additional developments are implemented in this version, including surface data assimilation, the inclusion of reflectivity as an analysis variable, and OL reflectivity updates.

Radar DA experiments are conducted using a two-step cycling strategy following Tong et al. (2016), as illustrated in Figure 2. In the first step, a 6-hourly cycled conventional DA experiment is performed, in which only non-radar observations are assimilated. This experiment is initialized from the ECMWF HRES deterministic analysis at 00 UTC 16 September 2024. After a 6-h spin-up, non-radar observations within a 6-h time window (±3 h) are assimilated every 6 hours continuously from 06 UTC 16 to 00 UTC 26 September 2024. In parallel with the conventional DA experiment, a series of hourly cycled radar DA experiments are initialized at time *T*. For each radar DA experiment, the background for the first DA cycle is provided by a 6-h forecast initialized from the conventional DA analysis at *T* - 6. Subsequently, both non-radar and radar data are assimilated hourly for 18 hours. From *T* + 6 onward, 12-h extended forecasts are launched every 3 hours util *T* + 18. To improve the large-scale states, blending is applied in both the conventional and radar DA experiments every 6 hours by blending the large-scale states from ECMWF HRES analyses with the small-scale states from MPAS-JEDI backgrounds.

To provide ensemble-based BECs for the 6-hourly conventional DA and hourly radar DA experiments, 32-member, 3-km ensemble forecasts are initialized from ECMWF ensemble analyses every 6 hours during the period from 00 UTC 16 to 00 UTC 26 September, 2024, with boundary conditions provided by the ECMWF ensemble forecasts. For the conventional DA experiment, 6-hour ensemble forecasts are used to construct the ensemble-based BECs. For the radar DA experiment, hourly ensemble-based BECs are derived from the 6–11-h ensemble forecasts at hourly intervals, covering the six hourly cycles every 6 hours. Owing to sampling errors associated with the limited ensemble size, covariance localization is applied. Horizontal localization scales of 300 km and 90 km are used for non-cloud variables (*U, V, T, Qv*, and *Ps*) and cloud variables (hydrometeors and reflectivity), respectively, while a vertical localization scale of 4 km is applied to all variables. In addition, the 6-h ensemble forecasts over the one-month period are used to train the static BEC model, from which the horizontal and vertical length scales, standard deviations, and multivariable correlations are estimated. With the static BEC available, the hybrid BEC is employed in the conventional DA, using a 60% ensemble-based BEC and 40% static BEC combination. The ensemble-based BEC localization and weighting parameters for conventional DA are determined from previous DA setup for this deep tropical region.

https://doi.org/10.5194/egusphere-2026-2476
Preprint. Discussion started: 29 May 2026

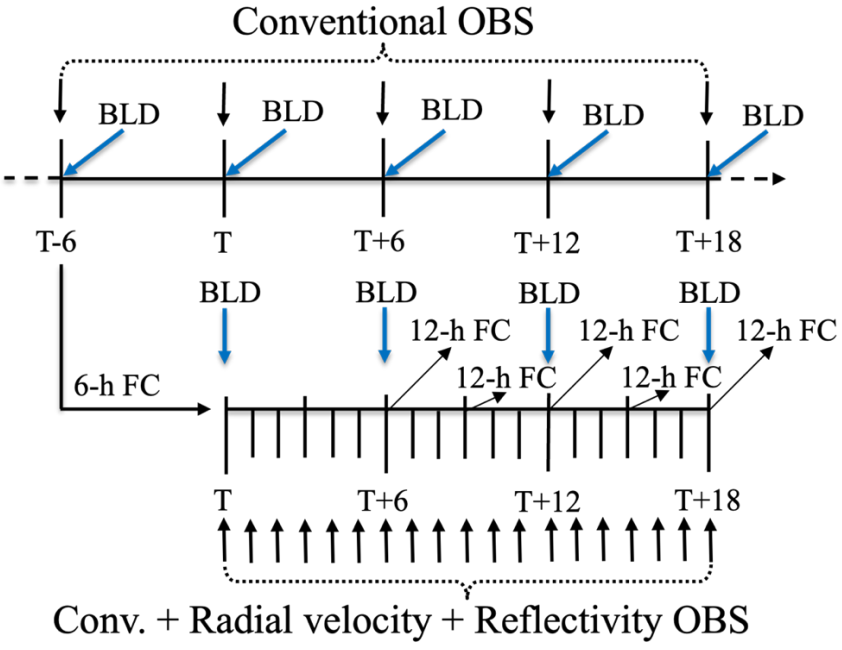

Figure 2. Flowchart of the 6-hourly conventional DA and hourly radar DA experiments. Conv. denotes conventional, OBS observations, BLD blending, and FC forecast. T indicates the time of the first radar DA cycle, for which the background is provided by the 6-h forecast from the conventional DA cycle at T-6. From T+6, 12-h forecasts are initialized from the radar DA analyses every three hours until T+18.

Radar DA experiments initialized at different times *T* constitute different case studies, following the cycling strategy illustrated in Fig 2. A total of five cases in September 2024 were selected, as summarized in Table 2. Among these, the Sumatra squall-line on 17 September 2024 is examined in detail to demonstrate the effectiveness of the direct reflectivity assimilation scheme. All five cases are then used for quantitative evaluation to assess the effectiveness of employing multivariate BEC in direct reflectivity assimilation on improving short-range heavy rainfall prediction.

Table 2. List of selected cases in radar DA experiments

Cases	Time of first radar DA cycle	Time of last radar DA cycle
17 September	18 UTC 16 Sept. 2024	12 UTC 17 Sept. 2024
23 September	18 UTC 22 Sept. 2024	12 UTC 23 Sept. 2024
24 September	18 UTC 23 Sept. 2024	12 UTC 24 Sept. 2024
25 September	18 UTC 24 Sept. 2024	12 UTC 25 Sept. 2024
26 September	12 UTC 25 Sept. 2024	06 UTC 26 Sept. 2024

https://doi.org/10.5194/egusphere-2026-2476
Preprint. Discussion started: 29 May 2026

For the Sumatra squall-line case study, four radar DA experiments were conducted (Table 3). In EnsB, a hybrid BEC, comprising 60% ensemble-based BEC and 40% static BEC, was used for non-cloud analysis variables, whereas a pure ensemble-based BEC was applied to the cloud variables. In the remaining experiments, a hybrid BEC (60% ensemble-based BEC and 40% static BEC) is applied to all variables. Two OLs are employed in both NoOLZH and 2OLZH. In NoOLZH, the reflectivity state is not updated before the second OL, whereas in 2OLZH, the reflectivity state is updated from the analyzed hydrometeors prior to the second OL. Both EnsB and HybB employ three OLs and update reflectivity before each OL. Comparisons among NoOLZH, 2OLZH, and HybB are designed to evaluate the impact of OL update of reflectivity on direct reflectivity assimilation. The comparison between EnsB and HybB further assesses the impact of MBE on direct reflectivity assimilation and short-range rainfall forecasts, based on both the Sumatra squall-line case study and multi-case quantitative evaluation. It should be noted that the static BEC is not specifically tuned for direct reflectivity assimilation, in order to ensure a fair comparison.

Table 3. Configuration of radar DA experiments.

Experiment	Reflectivity and hydrometeor BEC	Number of OLs	OL update of reflectivity
EnsB	100% ensemble-based BEC	3	Yes
HybB	60% ensemble-based BEC and 40% MBE	3	Yes
NoOLZh	60% ensemble-based BEC and 40% MBE	2	No
2OLZh	60% ensemble-based BEC and 40% MBE	2	Yes

4. MBE statistics and single observation experiments

In this section, the multivariate BEC statistics are first analyzed to assess whether cross-variable correlations are properly represented in the static BEC. Subsequentially, a series of single reflectivity observation assimilation experiments is conducted to evaluate whether the MBE can effectively propagate the reflectivity information across different model variables.

4.1 MBE statistics

The BEC characteristics are estimated from 3872 samples derived from 32-member ensemble forecast perturbations, generated over a one-month period with four cycles per day. The regression coefficients of $\delta T_u - \delta Q_u$, $\delta T_u - \delta Z_h$, and $\delta Q_u - \delta Z_h$ correlations are shown in Fig. 4 at a location near 1.5ºN latitude. The correlation structure between δT_u and δQ_u is predominantly diagonal, indicating strong vertical coupling between temperature and specific humidity increments (Fig. 3a). These two variables are negatively correlated throughout most of the column, indicating that a negative moisture increment (δQ) at a given level tends to be balanced by a positive temperature increment (δT) at the same level to maintain thermodynamic stability, and vice versa. Similarly, δT_u and δZ_h exhibit predominantly negative correlations, suggesting that

https://doi.org/10.5194/egusphere-2026-2476
Preprint. Discussion started: 29 May 2026

an increase in hydrometeors (positive δZ_h) is statistically linked to local cooling (negative δT), consistent with the evaporative cooling of precipitation or melting (Fig. 3b). However, above approximately model level 30 (~ 8 km), the correlation reverses sign, becoming positive. This upper-level positive correlation may indicate statistical links to processes where increased ice hydrometeors are associated with warming, such as through latent heat release during deposition. The most complex structure is seen in the $\delta Q_u - \delta Z_h$ correlation, which displays a distinct dipolar pattern in the vertical (Fig. 3c). Positive correlations are found slightly above a given reference level, while negative correlations appear slightly below it. This dipole structure is the statistical signature of the mass-conserving vertical exchange between water vapor and hydrometeors. Specifically, an increase in hydrometeors at one level (positive δZ_h) is linked to a decrease in moisture at/below that level (negative δQ) and an increase in moisture aloft (positive δQ), capturing the integrated vertical structure of condensation and its associated transport. This dipole's influence extends to the surface, where the negative correlation indicates that increased mid-level hydrometeors (e.g., rain aloft) are statistically linked to the reduced near-surface moisture, likely due to the evaporation of falling precipitation in dry downdrafts.

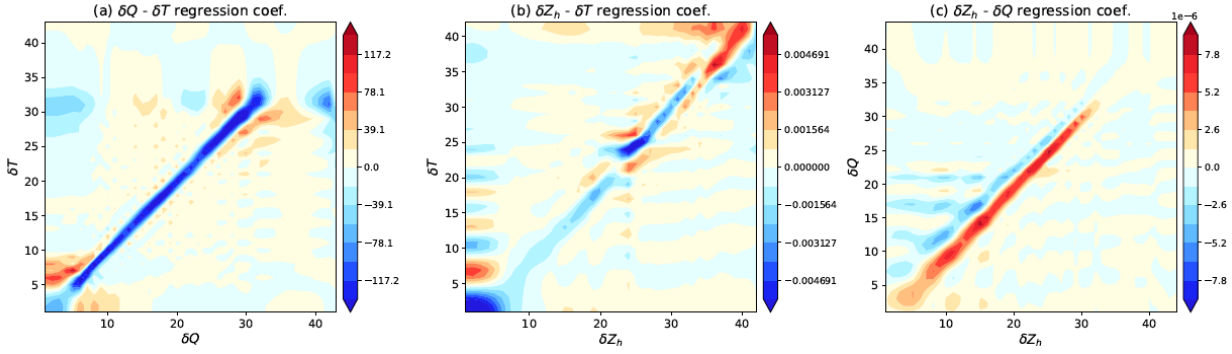

Figure 3. Regression coefficients near 1.5° N between (a) δT_u and δQ_u [K (kg kg-1)-1], (b) δT_u and δZ_h [K dBZ-1], and δQ_u and δZ_h [(kg kg-1) dBZ-1].

The regression correlations between hydrometeor increments and δZ_h are generally positively correlated throughout the vertical column. Instead of showing these regression correlations, we present the variance that can be predicted knowing δZ_h in Fig. 4, normalized by the total variance, for δQ_r, δQ_s, and δQ_g that are directly related to Z_h. These variance fractions exhibit clear variations with both latitude and vertical level. For δQ_r, up to 35% of the total variance can be explained by δZ_h below the model level 25, consistent with that rainwater is primarily confined to lower levels. For δQ_s, δZ_h explains over 50% of the variance between model level 25 and 43, and the variance fraction shows small variations with latitude and height, aligning with more extended vertical distribution of snow. For δQ_g, the predictive contribution of δZ_h is significant over similar levels as δQ_s, but the largest contributions occur above model level 30 and near 5° S and 10° N.

https://doi.org/10.5194/egusphere-2026-2476
Preprint. Discussion started: 29 May 2026

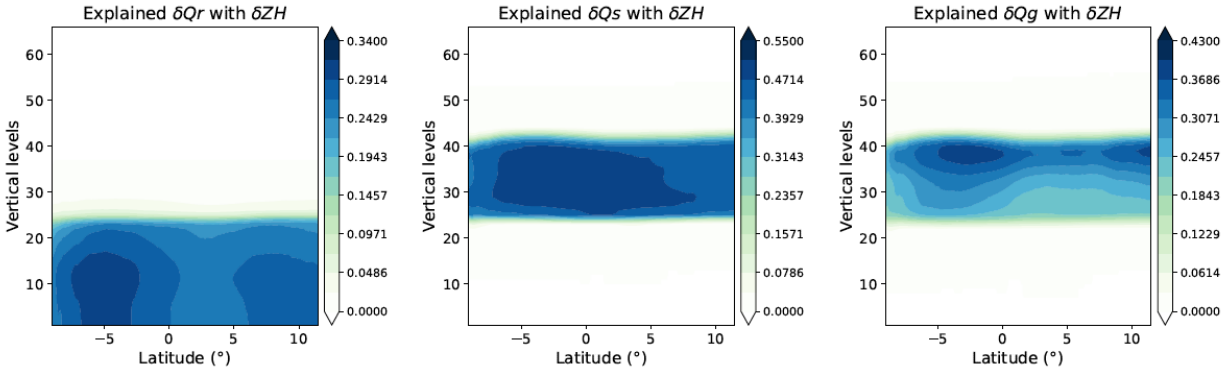

Figure 4. Ratio of balanced variance (i.e. that predicted by δZ_h) to total variance for (a) δQ_r, (b) δQ_s, and (c) δQ_g.

These cross-correlations between δZ_h and increments in temperature, humidity, and hydrometeors appear physically consistent, as evidenced by the MBE characteristics. This demonstrates that the multivariate correlations are properly established in the static BEC, allowing reflectivity information to be effectively propagated to other state variables during assimilation.

4.2 Single observation experiments

To investigate the DA system's response to the MBE for direct reflectivity assimilation, a series of single reflectivity assimilation experiments are conducted. A single reflectivity observation is placed at (1.5º N; 104º E) at a height of 3 km. The observation error standard deviation is set to 3 dBZ, and the innovation is fixed at 30 dBZ. Three assimilation experiments with different BEC configurations are designed: StaB using 100% static BEC, EnsB using 100% ensemble-based BEC, and HybB employing a hybrid BEC with 40% static and 60% ensemble-based components. Each experiment involves one OL, and reflectivity is updated from the final hydrometeor analyses.

Figure 5 shows the longitude-height cross sections of analysis increments for Z_h, T, and Q from three experiments along the latitude of 1.5ºN. In StaB, the increments of all three variables are broad in both horizontal and vertical directions, and the resulting structures are relatively smooth. Because Z_h is updated from the final hydrometeor analyses, its increment structure is not fully isotropic (Fig. 5a). The assimilation of a single reflectivity observation produces negative temperature increments below 6 km and positive increments above, as a response to the δT-δZ_h correlations established in the MBE (Fig. 5d). The humidity increment in StaB is positive throughout most of the column, as expected, except near the surface, where negative increments are generated in response to the negative δQ-δZ_h correlations between higher levels and near-surface levels (Fig.6g).

In EnsB, the Z_h increment is considerably more localized, and its magnitude even exceeds the innovation (Fig. 5b). With the pure ensemble-based BEC, the increments of T and Q spread broadly in the horizontal direction but remain narrowly confined in the vertical (Figs. 5e, h). In contrast to StaB, the assimilation of a single reflectivity observation warms the

https://doi.org/10.5194/egusphere-2026-2476
Preprint. Discussion started: 29 May 2026

surrounding air and adds moisture, while cooling the temperature and reducing humidity away from the observation in the upper and near-surface levels. As expected, the analysis increments of in HybB all three variables exhibit structures intermediate between those in StaB and EnsB, exhibiting moderate localization while retaining some degree of spatial smoothness, with magnitudes also laying between other two experiments (Figs. 5c, f, i).

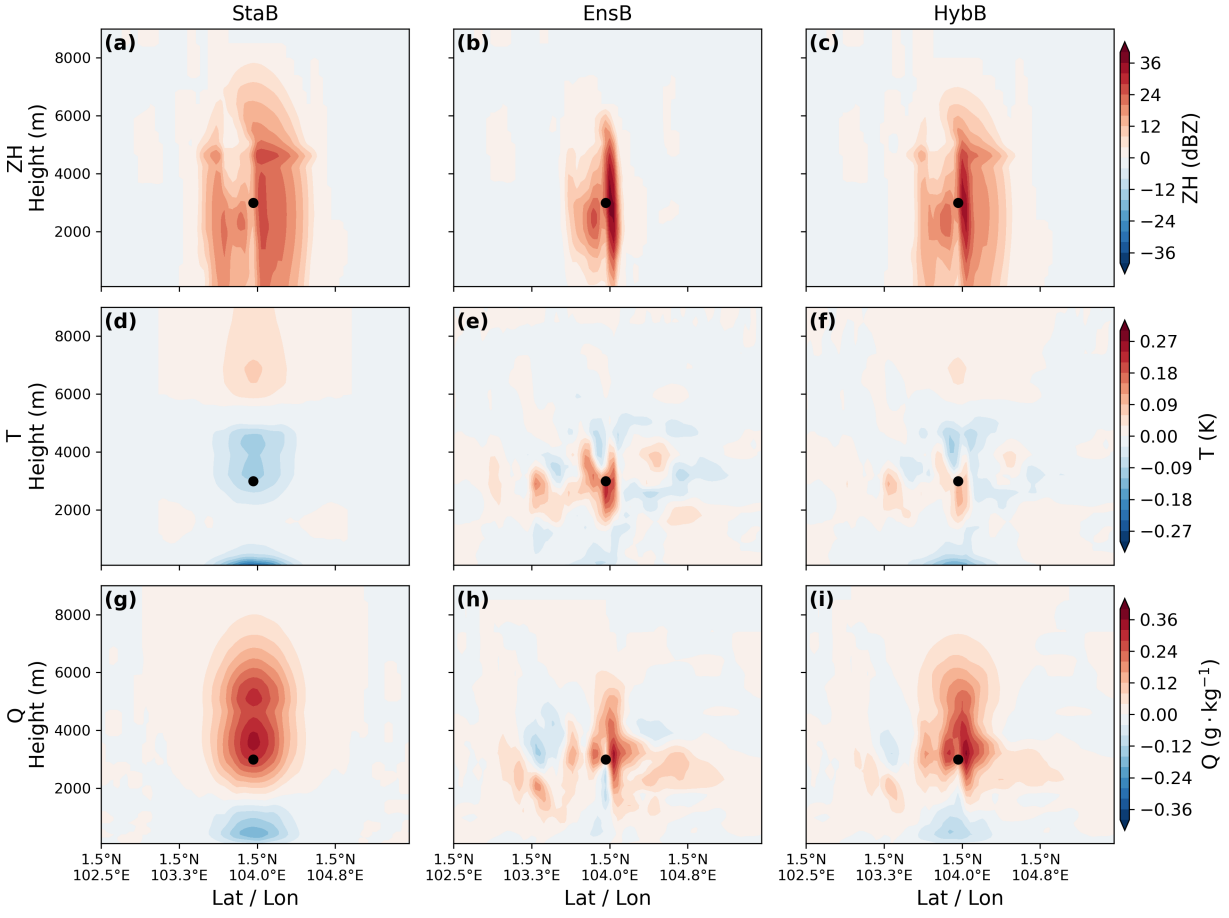

Figure 5. Height-longitude cross sections of analysis increment of (a-c) Z_h, (d-f) T, and (g-i) Q for (a, d, g) StaB, (b, e, h) EnsB, and (c, f, i) HybB. The cross sections are along the latitude of 1.5° N. The black dots indicate the location of the single reflectivity observation.

Figure 6 further shows the cross sections of analysis increments for three hydrometeors. Similar to Z_h, the hydrometeor increments in StaB are horizontally and vertically broad, showing a smooth and vertically deep and isotropic structure. Conversely, in EnsB, the increment of Q_r has a much larger magnitude, which explains the substantially larger Z_h increments obtained in EnsB. The increments of Q_s and Q_g in EnsB are much more localized in the vertical direction relative to StaB, with weaker Q_s increments and stronger Q_g increments. The hydrometeor increments in HybB lie between those in StaB and EnsB, showing intermediate magnitudes and spatial structures.

https://doi.org/10.5194/egusphere-2026-2476
Preprint. Discussion started: 29 May 2026

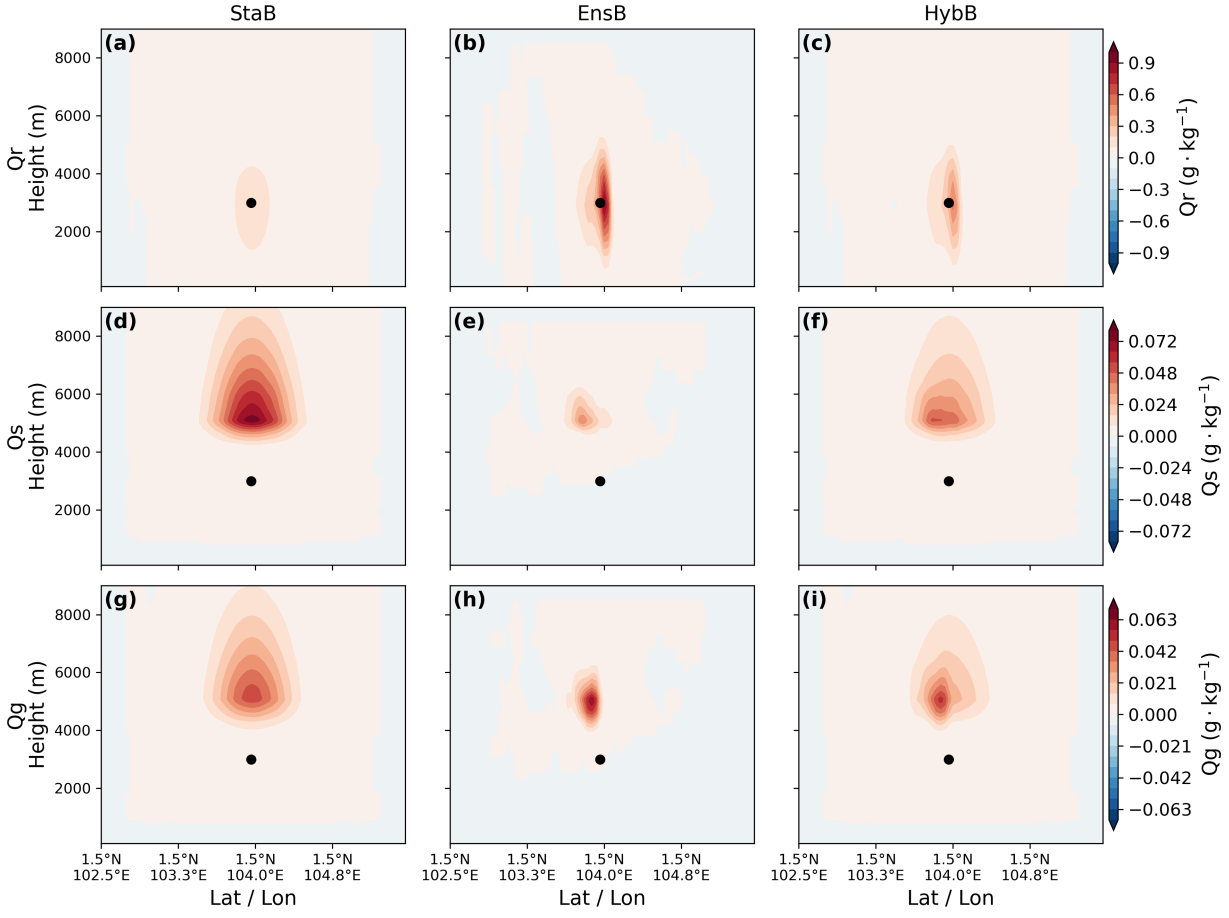

Figure 6. Similar to Fig. 5, but for (a-c) Q_r, (d-f) Q_s, and (g-i) Q_g.

Overall, the structure and magnitude of analysis increments for Z_h, T, Q, and hydrometeors reasonably reflect the characteristics of the BEC, whether static, ensemble-based, or hybrid. These single reflectivity assimilation experiments demonstrate the effective incorporation of MBE into the direct reflectivity assimilation within MPAS-JEDI's hybrid 3DEnVar.

5. Hourly cycled radar DA experiments

This section evaluates the effectiveness of the implemented direct reflectivity assimilation approach for short-range rainfall forecasting. The impacts of OL reflectivity update and the hybrid MBE on radar reflectivity assimilation and subsequent short-range forecasts are examined separately.

https://doi.org/10.5194/egusphere-2026-2476
Preprint. Discussion started: 29 May 2026

5.1 Impact of OL reflectivity updates

The impact of the OL reflectivity update on direct reflectivity assimilation is first examined through the Sumatra squall-line case on 17 September, 2024. Figure 7 shows the evolution of the cost function and the norm of its gradient as functions of inner-loop iterations, without and with OL reflectivity updates, for the assimilation of solely reflectivity data using two OLs at 1200 UTC 17 September. As expected, the cost function and gradient are identical in the first OL for both scenarios. Without OL update of reflectivity, only minimal increases in both the cost function and its gradient are observed at the beginning of the second OL, which can be attributed to the QC procedure permitting a small number of additional reflectivity observations to be assimilated. Both quantities then rapidly stabilize, indicating that the second OL introduces only minor adjustments to the model state. In contrast, when reflectivity is updated from the analyzed hydrometeor states, a substantially larger increase in both the cost function and its gradient is observed at the beginning of the second OL, followed by a gradual reduction as the minimization proceeds. The rise in the background term of the cost function suggests that the model state is significantly modified in the second OL, implying that direct reflectivity assimilation has a greater impact when OL reflectivity updates are included.

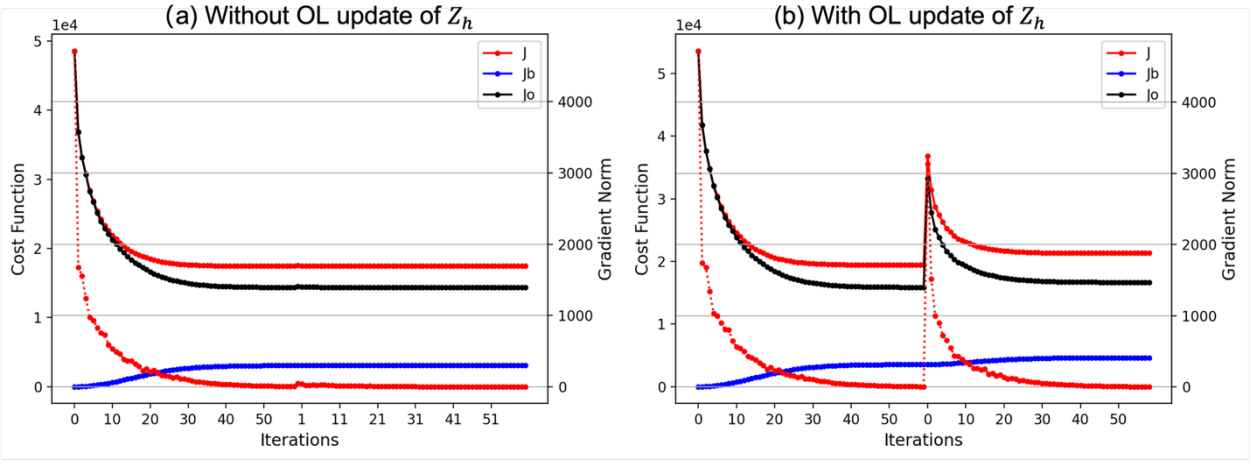

Figure 7. Evolution of the background term (Jb; solid blue), observation term (Jo; solid black), and total cost function (J; solid red), and the gradient norm of cost function (dashed red) as functions of inner-loop iterations during the two outer-loop minimizations of direct reflectivity assimilation: (a) without and (b) with OL reflectivity updates.

To assess whether the larger modifications to the model state introduced by OL reflectivity updates lead to improved fits to the observations, we examine the root-mean-square (RMS) of the differences between radar reflectivity observations and their model equivalents for the background, the guesses at the start of the second and third OLs, and the final analysis in HybB (Fig. 8). The RMS values are substantially reduced after direct reflectivity assimilation and decrease consistently as the number of OLs increases, indicating a progressively improved fit to the reflectivity observations when multiple OLs with reflectivity updates are employed. This improvement suggests that the hydrometeor state variables, in addition to reflectivity itself, are better constrained and more consistent with the observed reflectivity, indicating the effectiveness of OL reflectivity

https://doi.org/10.5194/egusphere-2026-2476
Preprint. Discussion started: 29 May 2026

updates in the direct reflectivity assimilation. For other observed quantities, OL reflectivity updates have only a minor impact, likely because their observation operators are comparatively linear.

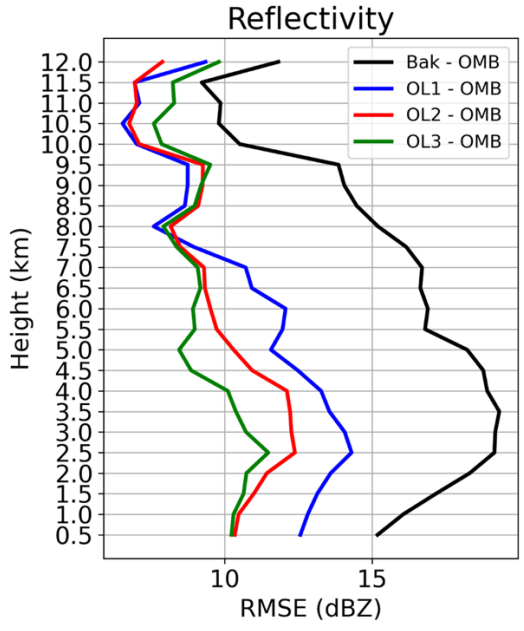

Figure 8. Vertical profiles of the root-mean-square (RMS) of differences between radar reflectivity observations and their model equivalents for the background (black), the guess at the start of the second OL (blue), the guess at the start of third OL (red), and the final analysis (green). The statistics are averaged over hourly data assimilation (DA) cycles from 18 UTC 16 to 09 UTC 17 September 2024 in HybB.

To further demonstrate the effectiveness of OL reflectivity updates for short-range rainfall forecasting, we compared the forecast skills of 1-12-h composite reflectivity for NoOLZh, 2OLZh, and HybB, as illustrated by the categorical performance diagrams (Roebber 2009) in Fig. 9. The performance diagram combines the probability of detection (POD), the critical success index (CSI), the frequency bias (BIAS), and the success ratio (one minus false alarm ratio (FAR)) in one diagram to evaluate the overall forecast performance. All scores are computed within a neighbourhood of 15 km radius to account for spatial displacement errors in the forecasts (Schwartz 2017). For the 20 dBZ threshold, both experiments that incorporate OL reflectivity updates outperform NoOLZh in the earlier forecast hours, indicating improved prediction of general convective coverage. Among the three, HybB exhibits the best forecast accuracy, with the green clusters located closer to the diagonal line and to the top-right corner, reflecting higher POD and CSI, and and a closer frequency bias to 1. For the 40 dBZ threshold, which emphasizes intense convective cores, 2OLZh shows improved accuracy relative to NoOLZh at early forecast lead times, but its performance degrades after approximately 6 hours. In contrast, HybB consistently demonstrates superior performance throughout most forecast lead times, with higher POD and CSI and fewer false alarms. These results highlight the added benefit of successive OL reflectivity updates in the direct reflectivity assimilation approach.

https://doi.org/10.5194/egusphere-2026-2476
Preprint. Discussion started: 29 May 2026

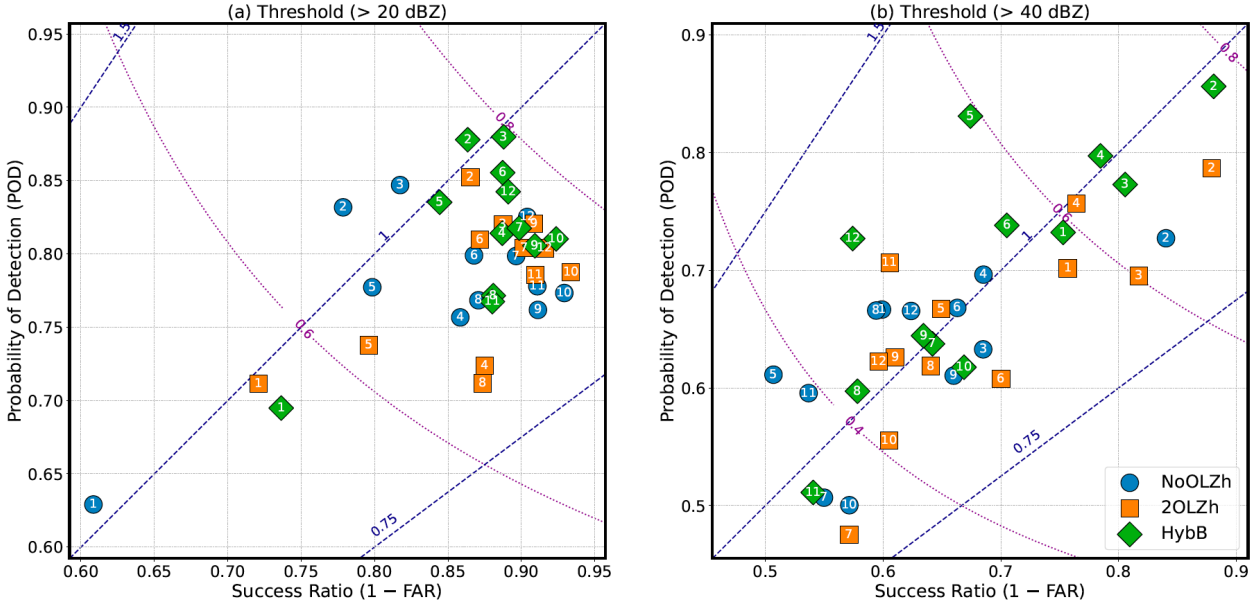

Figure 9. Neighborhood-based performance diagrams of 1-12-h composite reflectivity forecasts at thresholds of (a) 20 dBZ and (b) 40 dBZ for NoOLZh, 2OLZh, and HybB. Scores were aggerated over four assimilation cycles from 0000 to 1200 UTC 17 September at 3-h intervals, using a score radius of 15 km. The navy and purple lines indicate the frequency bias and critical success index, respectively.

5.2 Impact of hybrid multivariate BEC

In the following, we further evaluate the impacts of MBE on direct reflectivity assimilation through detailed study of the Sumatra squall line case and quantitative evaluations of multiple heavy rainfall cases.

5.2.1 Sumatra squall line case study

Figure 10 shows the vertical profiles of RMS of observation minus background (OMB) and observation minus analysis (OMA), averaged over 19 DA cycles for the Sumatra squall line case. For reflectivity, the inclusion of MBE substantially reduces the RMS values of OMA throughout the entire vertical column, and this improvement leads to consistently smaller OMB errors in HybB between 2 km and 7 km. The relatively larger RMS values of OMA in EnsB suggest imsufficient ensemble spread in the ensemble-based BEC. In contrast, the reduced RMS values in HybB highlight the advantages of employing a hybrid BEC in direct reflectivity assimilation. The positive impact on the reflectivity analysis further propagates to the wind fields through successive DA cycles. This is indicated by the slightly lower RMS values of both OMA and OMB in most levels between the height of 5 km and 10 km in HybB compared to EnsB.

https://doi.org/10.5194/egusphere-2026-2476
Preprint. Discussion started: 29 May 2026

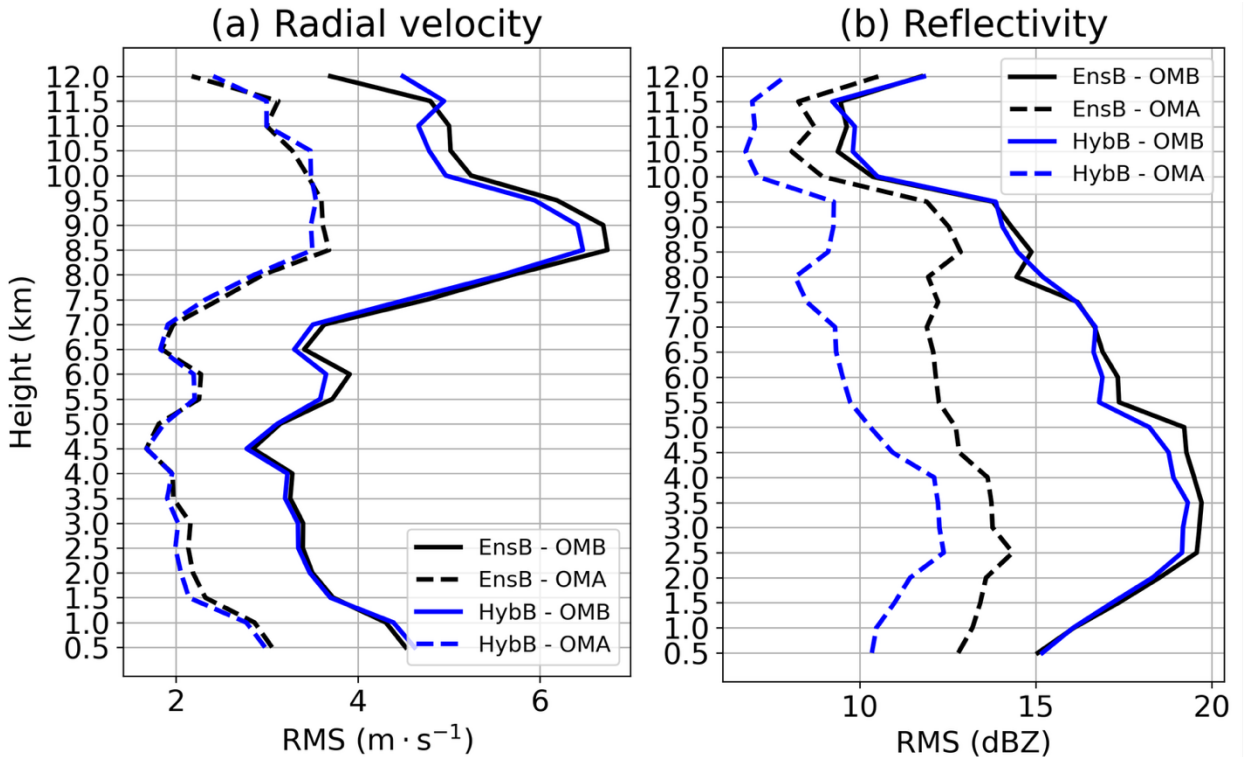

Figure 10. Vertical profiles of the RMS of observation-minus-background (OMB; solid lines) and observation-minus-analysis (OMA; dashed lines) for (a) radial velocity and (b) reflectivity. The statistics are averaged over DA cycles from 18 UTC 16 to 09 UTC 17 September 2024 at hourly intervals for EnsB (black curves) and HybB (blue curves).

Figure 11 presents the performance diagrams for the 1–12-h composite reflectivity forecast from EnsB and HybB. For the 20-dBZ threshold, the two experiments exhibit comparable forecast accuracy, although HybB shows slightly smaller biases and marginally higher CSI scores. For the 40-dBZ threshold, a larger fraction of the HybB points (orange) are clustered closer to the diagonal line and the upper-right corner of the diagram than those from EnsB (blue), indicating a improvement in the prediction of intense reflectivity by HybB relative to EnsB at an approximately 12-h forecasting lead time.

https://doi.org/10.5194/egusphere-2026-2476
Preprint. Discussion started: 29 May 2026

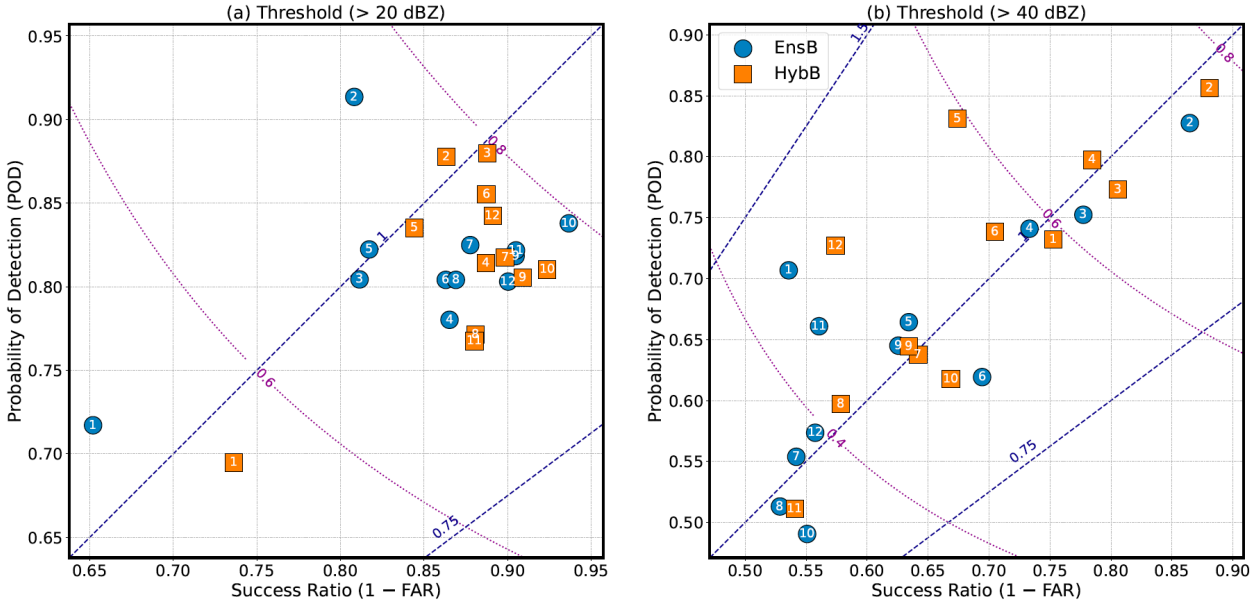

Figure 11. Similar to Fig. 9, but for EnsB and HybB.

Figure 12 compares the 3–6 h composite reflectivity forecasts initialized at 0600 UTC on 17 September 2024 for EnsB and HybB. Both experiments successfully predict the initialized convective storms at 0900 UTC, although location errors are observed. By 1000 UTC, the convective system develops into a north–south-oriented line, with EnsB producing slightly higher density along the line. The system further intensifies at 1100 UTC and reaches its mature stage by 1200 UTC. However, in EnsB, the squall-line system is poorly maintained, characterized by weakened reflectivity intensity and a fragmented linear structure, particularly in the northern portion of the line over the sea and Malaysia. In contrast, HybB shows clear improvements in both the orientation and propagation of the squall line, producing a more coherent and persistent structure with stronger leading-edge reflectivity structure, despite missing the far northern part of the line system over Malaysia at 1200 UTC.

https://doi.org/10.5194/egusphere-2026-2476
Preprint. Discussion started: 29 May 2026

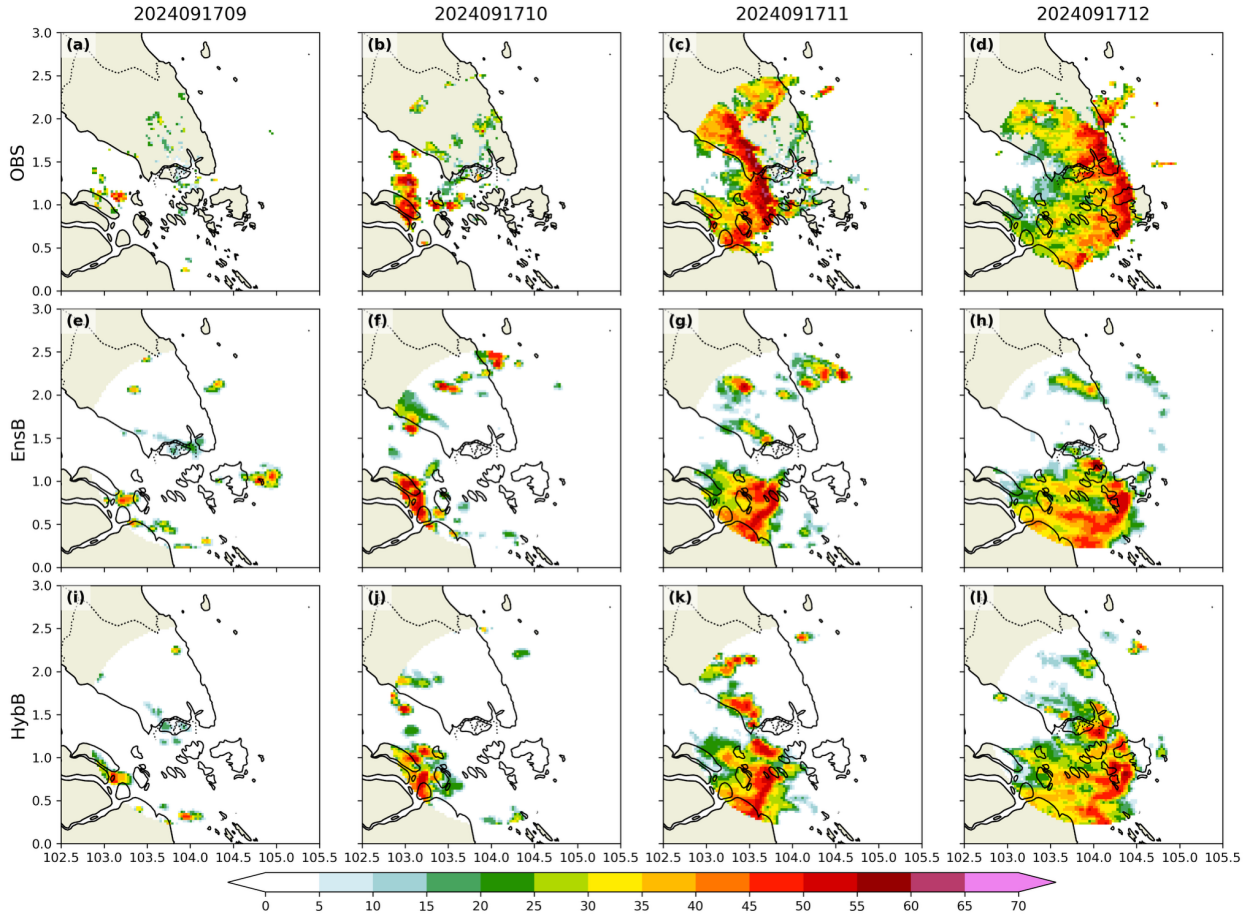

Figure 12. Composite reflectivity valid at 09, 10, 11, and 12 UTC on 17 September 2024. The first row shows observations, and the second and third rows show forecasts initialized at 06 UTC 17 September for EnsB and HybB, respectively.

5.2.2. Multiple case evaluation

We further perform quantitative evaluations across multiple severe weather cases to assess the impact of incorporating the MBE into direct reflectivity assimilation on short-range severe weather forecasts over Singapore. Composite reflectivity and 3-h accumulated precipitation forecasts from EnsB and HybB are verified against radar reflectivity observations and radar-derived quantitative precipitation estimates (QPE). Five severe weather cases are examined, with each case consisting of 12-hour forecasts initialized from radar DA analyses from five cycles at 3-hour intervals, yielding a total of 25 forecast samples for verification.

Figure 13 shows the performance diagram of 1–12-h composite reflectivity forecasts at thresholds of 20 and 40 dBZ. At the 20-dBZ threshold, HybB outperforms EnsB during approximately the first 7 hours, exhibiting higher forecast accuracy, after which its performance becomes comparable to or slightly worse than that of EnsB. The benefits of incorporating a hybrid MBE in direct reflectivity assimilation are more evident at the higher 40-dBZ threshold. HybB obtains higher POD, lower

https://doi.org/10.5194/egusphere-2026-2476
Preprint. Discussion started: 29 May 2026

FAR, and higher CSI values throughout the entire 12-h forecast period. The improvement is illustrated by the orange rectangles clustering closer to the top-right corner of the performance diagram than the blue circles at all forecast lead times.

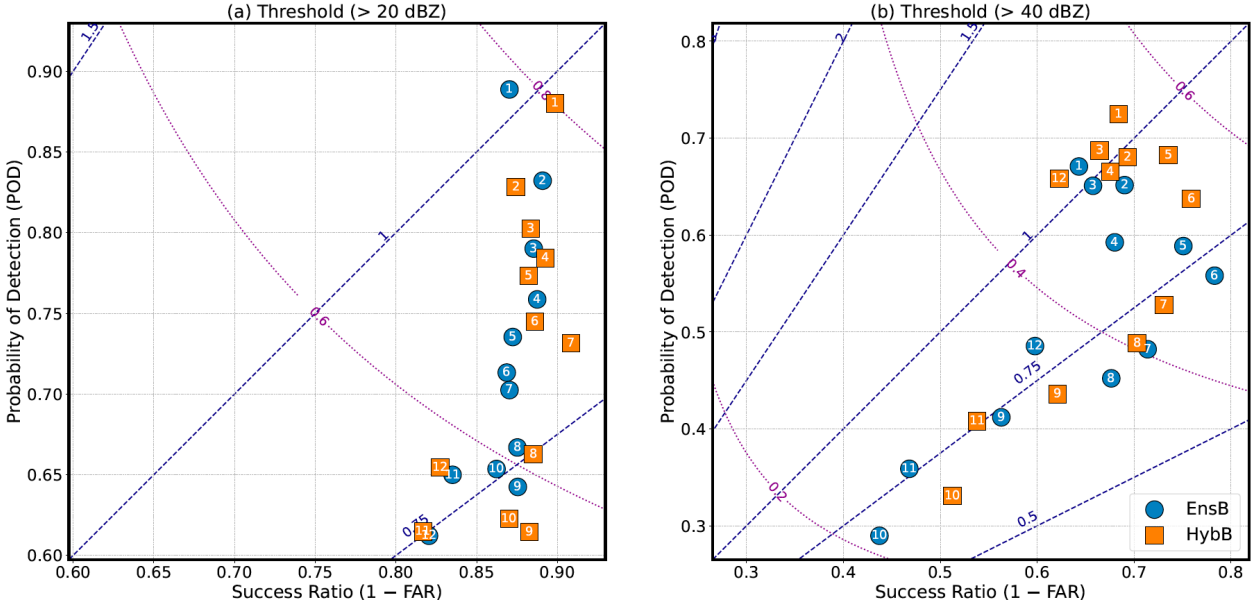

Figure 13. Similar to Fig. 10, but for EnsB and HybB. Statistics are aggregated from 25 forecast samples, consisting of five cases, each with five 12-hour forecast cycles.

Quantitative precipitation forecast (QPF) skill provides an additional measure of the forecast impact of incorporating MBE into direct reflectivity assimilation. We compare the Fractions skill score (FSS) and frequency bias for 3-h accumulated precipitation forecasts in EnsB and HybB in Figure 14. Overall, HybB consistently achieves higher FSS values across most forecast lead times and thresholds, indicating improved spatial agreement with radar-derived QPE, particularly during the early forecast hours. The advantage of HybB is most pronounced at the higher threshold of 15 mm, suggesting that the inclusion of MBE is especially beneficial for forecasting heavier precipitation associated with intense convective systems. In terms of frequency bias, both experiments show a general tendency toward decreasing bias with forecast lead time; however, HybB remains closer to the value of 1.0 than EnsB across all thresholds, reflecting a more accurate representation of precipitation coverage and intensity.

https://doi.org/10.5194/egusphere-2026-2476
Preprint. Discussion started: 29 May 2026

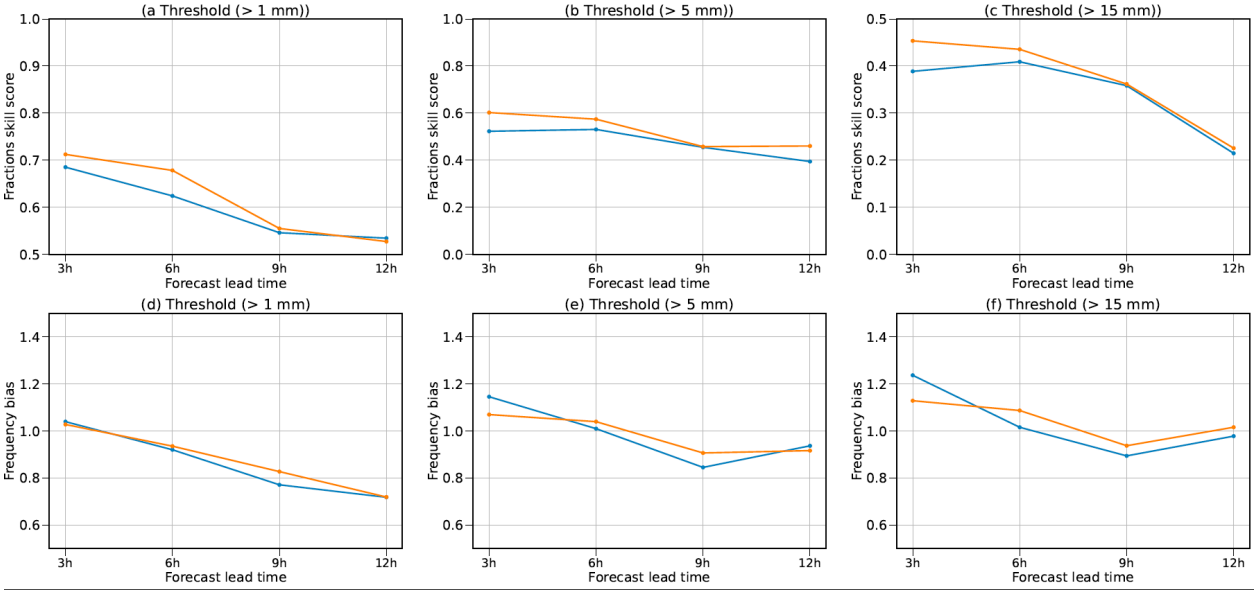

Figure 14. Time series of (a–c) fractions skill score (FSS) and (d–f) frequency bias for 3-h accumulated precipitation forecasts at the thresholds of (a, d) 1 mm, (b, e) 5 mm, and (c, f) 15 mm. Statistics are aggregated from 25 forecast samples, consisting of five cases, each with five 12-hour forecast cycles. The neighbourhood score radius is 25 km.

Overall, the multi-case quantitative evaluation demonstrates that incorporating MBE into the static component of BEC provides additional benefits over a purely ensemble-based BEC in direct reflectivity assimilation. These improvements are reflected in enhanced forecast skill for both composite reflectivity and 3-hour accumulated precipitation, highlighting the positive impact of MBE on short-range severe weather prediction.

6. Conclusions

In this study, we implement a direct reflectivity assimilation approach within the MPAS-JEDI hybrid 3DEnVar, following Wang and Wang (2017, 2021), in which reflectivity is treated as an analysis variable. The static BEC is carefully designed to explicitly incorporate key cross-variable correlations between reflectivity and temperature, humidity, and hydrometeor mixing ratios, allowing reflectivity information to propagate to thermodynamic and hydrometeor increments through the static BEC component. In addition, an OL reflectivity update is applied, whereby the reflectivity state is recomputed from analyzed hydrometeors in successive OLs, allowing the model state to progressively better match the observed reflectivity. The performance of the implemented direct reflectivity assimilation is evaluated through hourly cycled radar assimilation for heavy rainfall cases in the deep tropics.

We first examine the characteristics of the multivariate correlations in the MBE. The diagnosed cross-variable correlations indicate that the MBE captures physically consistent relationships between reflectivity and thermodynamic and hydrometeors variables. Single observation experiments further confirm that the reflectivity assimilation effectively induces

https://doi.org/10.5194/egusphere-2026-2476
Preprint. Discussion started: 29 May 2026

consistent increments in temperature, humidity, and hydrometeors, in agreement with the diagnosed multivariate correlations.

Using a Sumatra squall-line case on 17 September 2024, we show that OL reflectivity updates progressively adjust the model state variables, allowing the analysed reflectivity and hydrometeors to better match the observed reflectivity observations and leading to improved squall-line forecasts. The inclusion of MBE further improves the fit of both background and analysis to radar radial velocity and reflectivity observations. Consequently, the squall-line prediction exhibits improved orientation, stronger intensity, and a more organized structure. Multi-case evaluations further demonstrate that MBE provides added value beyond a purely ensemble-based BEC, yielding enhanced forecast accuracy in both composite reflectivity and 3-h accumulated precipitation.

Although these results are encouraging, several limitations remain. First, the ensemble-based BEC is derived from cold-start ensembles initialized from ECMWF ensemble analyses, which is suboptimal. Implementing a fully coupled ensemble DA system (e.g. MPAS-JEDI's LGETKF; Sun et al. 2025) alongside the current hybrid 3DEnVar is expected to further improve direct reflectivity assimilation and short-range forecasts. Second, a relatively larger localization scale (i.e., 300 km) is applied to non-cloud variables, which may not be optimal for the radial velocity assimilation. Further work will investigate scale-dependent localization (Buehner 2012; Buehner and Shlyaeva 2015; Huang et al. 2021) to enable more effective multiscale assimilation of both conventional and radar observations. In addition, only Singapore radars are assimilated in this study, limiting the impact primarily to the surrounding region. Incorporating radar observations from neighbouring networks could extend the benefits (Ridal and Dahlbom 2017). Further evaluation of the direct reflectivity assimilation in regions with denser radar networks is also worth pursuing. These directions will be explored in future work.

Code and data availability

The source code of MPAS-JEDI 3.0.3 is available on Zenodo at https://doi.org/10.5281/zenodo.19209009 (last access: 1 May 2026; JCSDA and NCAR 2023). The source code of MPAS-A 8.3.1 is available on Zenodo at https://doi.org/10.5281/zenodo.15686368 (last access: 1 May 2026; Duda et al. 2025). Conventional and GNSS RO observations were obtained from the NCAR Research Data Archive (RDA) https://rda.ucar.edu/datasets/d337000 (last access: 1 May 2025; National Centers For Environmental Prediction/National Weather Service/NOAA/U.S. Department Of Commerce, 2008) and https://rda.ucar.edu/datasets/d735000 (last access: 1 May 2026; National Centers For Environmental Prediction/National Weather Service/NOAA/U.S. Department Of Commerce, 2009). Radar observations, ECMWF deterministic and ensemble analyses were provided by CCRS and are available from the corresponding author upon request.

https://doi.org/10.5194/egusphere-2026-2476
Preprint. Discussion started: 29 May 2026

Author contributions

TS designed, conducted, and analysed all experiments and wrote the manuscript. IC configured the MPAS model and generated the background error samples. CSS implemented the blending approach. LZ, HZ, and DB aided with experimental design and analysis. All authors contributed to the discussion of the results and reviewed and revised the manuscript.

Competing interests

The authors have no competing interests.

Acknowledgements

This work was conducted under the collaboration between the Centre for Climate Research Singapore (CCRS), Singapore, and the National Science Foundation National Center for Atmospheric Research (NCAR), United States. The numerical calculations were supported by the National Supercomputing Centre (NSCC), Singapore, and NCAR's Computational and Information Systems Laboratory (CISL). The first author gratefully acknowledges Yongming Wang and Xuguang Wang from the University of Oklahoma, United States, for their early prototype implementation within MPAS-JEDI, which helped motivate this study.

References

Buehner, M., and A. Shlyaeva: Scale-dependent background-error covariance localisation. Tellus, 67A, 28027, https://doi.org/10.3402/tellusa.v67.28027, 2015.

Buehner, M.: Evaluation of a spatial/spectral covariance localization approach for atmospheric data assimilation. Mon. Wea. Rev., 140, 617–636, https://doi.org/10.1175/MWR-D-10-05052.1, 2012.

Chen, L., Liu, C., Xue, M., Zhao, G., Kong, R., & Jung, Y.: Use of Power Transform Mixing Ratios as Hydrometeor Control Variables for Direct Assimilation of Radar Reflectivity in GSI En3DVar and Tests with Five Convective Storm Cases. Monthly Weather Review, 149(3), 645-659. https://doi.org/10.1175/MWR-D-20-0149.1, 2021.

Courtier, P., Thépaut, J.-N. & Hollingsworth, A.: A strategy for operational implementation of 4d-var, using an incremental approach. Quarterly Journal of the Royal Meteorological Society, 120(519), 1367–1387, https://doi.org/10.1002/qj.49712051912, 1994.

Duda, M., Jacobsen, D., Petersen, M., Hoffman, M., ldfowler58, Turner, A. K., Asay-Davis, X., Ringler, T., Roekel, L. V., Curry, M., Lipscomb, W., Dickerson, G. D., stephenprice, skamaroc, Jeffery, N., Heinzeller, D., Woodring, J., Wolfram, P. J., maltrud, Saenz, J., Abishek, Jim W., mdtoyNOAA, Nick, weiwangncar, Mametjanov, A., mperego, Werner, K., Wang,

https://doi.org/10.5194/egusphere-2026-2476
Preprint. Discussion started: 29 May 2026

K.C., Wolfe, J.: MPAS-Dev/MPAS-Model: MPAS Version 8.3.1 (v8.3.1). Zenodo. [code], https://doi.org/10.5281/zenodo.15686368, 2025.

Evensen, G.: Sequential data assimilation with a nonlinear quasi-geostrophic model using Monte Carlo methods to forecast error statistics, J. Geophys. Res., 99(C5), 10143–10162, https://doi.org/10.1029/94JC00572, 1994.

Gao, J., and D. J. Stensrud: Assimilation of Reflectivity Data in a Convective-Scale, Cycled 3DVAR Framework with Hydrometeor Classification. J. Atmos. Sci., 69, 1054–1065, https://doi.org/10.1175/JAS-D-11-0162.1, 2012.

Gao, S., Chen, J., Yu, C., Hu, H. & Wu, Y.: Direct assimilation of radar reflectivity using an ensemble 3DEnVar approach to improve analysis and forecasting of tornadic supercells over eastern China. Quarterly Journal of the Royal Meteorological Society, 150(762), 2581–2601. https://doi.org/10.1002/qj.4724, 2024.

Grell, G. A., and S. R. Freitas: A Scale and Aerosol Aware Stochastic Convective Parameterization for Weather and Air Quality Modeling. Atmos. Chem. Phys., 14, 5233–5250, https://doi.org/10.5194/acp-14-5233-2014, 2014.

Hong, S.-Y., and J.-O. J. Lim: The WRF Single–Moment 6–Class Microphysics Scheme (WSM6). J. Korean Meteor. Soc., 42, 129–151, 2006.

Huang, B., X. Wang, D. T. Kleist, and T. Lei: A Simultaneous Multiscale Data Assimilation Using Scale-Dependent Localization in GSI-Based Hybrid 4DEnVar for NCEP FV3-Based GFS. Mon. Wea. Rev., 149, 479–501, https://doi.org/10.1175/MWR-D-20-0166.1, 2021.

Iacono, M. J., J. S. Delamere, E. J. Mlawer, M. W. Shephard, S. A. Clough, and W. D. Collins: Radiative Forcing by Long–Lived Greenhouse Gases: Calculations with the AER Radiative Transfer Models. J. Geophys. Res., 113, D13103, https://doi.org/10.1029/2008JD009944, 2008.

Joint Center for Satellite Data Assimilation and National Center for Atmospheric Research: JEDI-MPAS Data Assimilation System v3.0.3 (3.0.3), Zenodo [code], https://doi.org/10.5281/zenodo.19209009, 2025.

Jung, B.-J., Ménétrier, B., Snyder, C., Liu, Z., Guerrette, J. J., Ban, J., Baños, I. H., Yu, Y. G., and Skamarock, W. C.: Three-dimensional variational assimilation with a multivariate background error covariance for the Model for Prediction Across Scales – Atmosphere with the Joint Effort for Data assimilation Integration (JEDI-MPAS 2.0.0-beta), Geosci. Model Dev., 17, 3879–3895, https://doi.org/10.5194/gmd-17-3879-2024, 2024.

Liu, C., Li, H., Xue, M., Jung, Y., Park, J., Chen, L., Kong, R., & Tong, C.-C.: Use of a Reflectivity Operator Based on Double-Moment Thompson Microphysics for Direct Assimilation of Radar Reflectivity in GSI-Based Hybrid En3DVar. Monthly Weather Review, 150(4), 907-926. https://doi.org/10.1175/MWR-D-21-0040.1, 2022.

Liu, C., Xue, M., & Kong, R.: Direct Variational Assimilation of Radar Reflectivity and Radial Velocity Data: Issues with Nonlinear Reflectivity Operator and Solutions. Monthly Weather Review, 148(4), 1483-1502. https://doi.org/10.1175/MWR-D-19-0149.1, 2020.

Liu, P., J. Gao, G. Zhang, and J. T. Carlin: Direct Assimilation of Polarimetric Radar Data with a Variational Approach Using Both Mixing Ratio and Total Number Concentration as Analysis Variables: Observing System Simulation Experiments. Mon. Wea. Rev., 154, 79–98, https://doi.org/10.1175/MWR-D-24-0264.1, 2025.

https://doi.org/10.5194/egusphere-2026-2476
Preprint. Discussion started: 29 May 2026

Liu, P., Zhang, G., Carlin, J. T., & Gao, J.: Direct assimilation of radar reflectivity data in logarithmic scale or power transform? Geophysical Research Letters, 52, e2025GL116531. https://doi.org/10.1029/2025GL116531, 2025.

Liu, Z., Snyder, C., Guerrette, J. J., Jung, B.-J., Ban, J., Vahl, S., Wu, Y., Trémolet, Y., Auligné, T., Ménétrier, B., Shlyaeva, A., Herbener, S., Liu, E., Holdaway, D., and Johnson, B. T.: Data assimilation for the Model for Prediction Across Scales – Atmosphere with the Joint Effort for Data assimilation Integration (JEDI-MPAS 1.0.0): EnVar implementation and evaluation, Geosci. Model Dev., 15, 7859–7878, https://doi.org/10.5194/gmd-15-7859-2022, 2022.

National Centers for Environmental Prediction/National Weather Service/NOAA/U.S. Department of Commerce: NCEP ADP Global Upper Air and Surface Weather Observations (PREPBUFR format), Research Data Archive at the National Center for Atmospheric Research, Computational and Information Systems Laboratory [data set], https://doi.org/10.5065/Z83F-N512, 2008.

National Centers for Environmental Prediction/National Weather Service/NOAA/U.S. Department of Commerce: NCEP GDAS Satellite Data 2004–continuing, Research Data Archive at the National Center for Atmospheric Research, Computational and Information Systems Laboratory [data set], https://doi.org/10.5065/DWYZ-Q852, 2009.

Olson, J. B., T. Smirnova, J. S. Kenyon, D. D. Turner, J. M. Brown, W. Zheng, and B. W. Green: A Description of the MYNN Surface-Layer Scheme. NOAA Tech. Memo OAR GSL-67, https://doi.org/10.25923/f6a8-bc75, 2021.

Ridal, M., and M. Dahlbom: Assimilation of Multinational Radar Reflectivity Data in a Mesoscale Model: A Proof of Concept. J. Appl. Meteor. Climatol., 56, 1739–1751, https://doi.org/10.1175/JAMC-D-16-0247.1, 2017.

Roberts N. M., Lean H. W.: Scale-Selective Verification of Rainfall Accumulations from High-Resolution Forecasts of Convective Events. Mon. Wea. Rev., 136, 78-97, https://doi.org/10.1175/2007MWR2123.1, 2008.

Roebber, P. J.: Visualizing Multiple Measures of Forecast Quality, Weather and Forecasting, 24, 601-608, https://doi.org/10.1175/2008WAF2222159.1, 2009.

Schwartz, C. S.: A comparison of methods used to populate neighborhood-based contingency tables for high-resolution forecast verification. Weather and Forecasting, 32(2), 733–741. https://doi.org/10.1175/WAF-D-16-0187.1, 2017.

Skamarock, W. C., Duda, M. G., Ha, S., and Park, S.-H.: Limited-Area Atmospheric Modeling Using an Unstructured Mesh, Mon. Weather Rev., 146, 3445–3460, https://doi.org/10.1175/mwr-d-18-0155.1, 2018.

Skamarock, W. C., Klemp, J. B., Duda, M. G., Fowler, L. D., Park, S.-H., and Ringler, T. D.: A Multiscale Nonhydrostatic Atmospheric Model Using Centroidal Voronoi Tessellations and C-Grid Staggering, Mon. Weather Rev., 140, 3090–3105, https://doi.org/10.1175/mwrd-11-00215.1, 2012.

Sun, J., and N. A. Crook: Dynamical and Microphysical Retrieval from Doppler Radar Observations Using a Cloud Model and Its Adjoint. Part I: Model Development and Simulated Data Experiments. J. Atmos. Sci., 54, 1642–1661, https://doi.org/10.1175/1520-0469(1997)054<1642:DAMRFD>2.0.CO;2, 1997.

Sun, J., H. Wang, W. Tong, Y. Zhang, C. Lin, and D. Xu: Comparison of the Impacts of Momentum Control Variables on High-Resolution Variational Data Assimilation and Precipitation Forecasting. Mon. Wea. Rev., 144, 149–169, https://doi.org/10.1175/MWR-D-14-00205.1, 2016.

https://doi.org/10.5194/egusphere-2026-2476
Preprint. Discussion started: 29 May 2026

Sun, J., M. Xue, J.W. Wilson, I. Zawadzki, S.P. Ballard, J. Onvlee-Hooimeyer, P. Joe, D.M. Barker, P. Li, B. Golding, M. Xu, and J. Pinto: Use of NWP for Nowcasting Convective Precipitation: Recent Progress and Challenges. Bull. Amer. Meteor. Soc., 95, 409–426, https://doi.org/10.1175/BAMS-D-11-00263.1, 2014.

Sun, T., Guerrette, J. J., Liu, Z., Ban, J., Jung, B.-J., Hernandez Banos, I., and Snyder, C.: All-sky AMSU-A radiance data assimilation using the gain-form of Local Ensemble Transform Kalman filter within MPAS-JEDI-2.1.0: implementation, tuning, and evaluation, Geosci. Model Dev., 18, 8569–8587, https://doi.org/10.5194/gmd-18-8569-2025, 2025.

Tewari, M., F. Chen, W. Wang, J. Dudhia, M. A. LeMone, K. Mitchell, M. Ek, G. Gayno, J. Wegiel, and R. H. Cuenca: Implementation and Verification of the Unified NOAH Land Surface Model in the WRF Model. 20th Conf. Weather Analysis and Forecasting/16th Conf. Numerical Weather Prediction, 11–15, 2004.

Trémolet, Y. and Auligné T.: The Joint Effort for Data Assimilation Integration (JEDI), JCSDA Quarterly Newsletter, 66, 1–5, https://doi.org/10.25923/RB19-0Q26, 2020.

Wang, H., J. Sun, S. Fan, and X. Huang: Indirect Assimilation of Radar Reflectivity with WRF 3D-Var and Its Impact on Prediction of Four Summertime Convective Events. J. Appl. Meteor. Climatol., 52, 889–902, https://doi.org/10.1175/JAMC-D-12-0120.1, 2013.

Wang, S. and Liu, Z.: A radar reflectivity operator with ice-phase hydrometeors for variational data assimilation (version 1.0) and its evaluation with real radar data, Geosci. Model Dev., 12, 4031–4051, https://doi.org/10.5194/gmd-12-4031-2019, 2019

Wang, Y., and X. Wang: Development of Convective-Scale Static Background Error Covariance within GSI-Based Hybrid EnVar System for Direct Radar Reflectivity Data Assimilation. Mon. Wea. Rev., 149, 2713–2736, https://doi.org/10.1175/MWR-D-20-0215.1, 2021.

Wang, Y., and X. Wang: Direct Assimilation of Radar Reflectivity without Tangent Linear and Adjoint of the Nonlinear Observation Operator in the GSI-Based EnVar System: Methodology and Experiment with the 8 May 2003 Oklahoma City Tornadic Supercell. Mon. Wea. Rev., 145, 1447–1471, https://doi.org/10.1175/MWR-D-16-0231.1, 2017.

Xiao, Q., Kuo, Y., Sun, J., Lee, W., Barker, D. M., & Lim, E.: An Approach of Radar Reflectivity Data Assimilation and Its Assessment with the Inland QPF of Typhoon Rusa (2002) at Landfall, Journal of Applied Meteorology and Climatology, 46(1), 14-22. https://doi.org/10.1175/JAM2439.1, 2007.

Xu, K., and D. A. Randall: A Semiempirical Cloudiness Parameterization for Use in Climate Models. J. Atmos. Sci., 53, 3084–3102, https://doi.org/10.1175/1520-0469(1996)053<3084:ASCPFU>2.0.CO;2, 1996.